Cancer Biol Med 2016. doi: 10.20892/j.issn.2095-3941.2016.0048

ORIGINAL ARTICLE

Near-infrared dye-loaded magnetic nanoparticles as photoacoustic contrast agent for enhanced tumor imaging

Chuang Gao[1 *], Zi-Jian Deng[1 *], Dong Peng[2], Yu-Shen Jin[3], Yan Ma[3], Yan-Yan Li[3], Yu-Kun Zhu[2], Jian-Zhong Xi[1], Jie Tian[2], Zhi-Fei Dai[1], Chang-Hui Li[1], Xiao-Long Liang[1]

[1]Department of Biomedical Engineering, College of Engineering, Peking University, Beijing 100871, China; [2]Institute of Automation, Chinese Academy of Sciences, Beijing 100190, China; [3]Nanomedicine and Biosensor Laboratory, School of Life Science and Technology, Harbin Institute of Technology, Harbin 150080, China

ABSTRACT

Objective: Photoacoustic (PA) tomography (PAT) has attracted extensive interest because of its optical absorption contrast and ultrasonic detection. This study aims to develop a biocompatible and biodegradable PA contrast agent particularly promising for clinical applications in human body.

Methods: In this study, we presented a PA contrast agent: 1, 2-distearoyl-sn-glycero-3-phosphoethanolamine-*N*-[methoxy (polyethylene glycol)] (DSPE-PEG)-coated superparamagnetic iron oxide (SPIO) nanoparticles (NPs) loaded with indocyanine green (ICG). We used ICG and SPIO NPs because both drugs are approved by the U.S. Food and Drug Administration. Given the strong absorption of near-infrared laser pulses, SPIO@DSPE-PEG/ICG NPs with a uniform diameter of ~28 nm could significantly enhance PA signals.

Results: We demonstrated the contrast enhancement of these NPs in phantom and animal experiments, in which the *in vivo* circulation time of SPIO@DSPE-PEG/ICG NPs was considerably longer than that of free ICG. These novel NPs also displayed a high efficiency of tumor targeting.

Conclusions: SPIO@DSPE-PEG/ICG NPs are promising PAT contrast agents for clinical applications.

KEYWORDS Indocyanine green; magnetic nanoparticles; photoacoustic tomography; tumor imaging

Introduction

Photoacoustic (PA) tomography (PAT) is a non-ionizing, non-invasive imaging modality based on PA effect[1,2]. Owing to its optical absorption contrast and ultrasonic detection, PAT has been widely applied in high-contrast anatomical and functional imaging of different tissues, such as brain structural and functional imaging, breast cancer imaging, and tumor angiogenesis monitoring[3-7]. PAT can use diffused photons to obtain high-resolution image of deep tissues unlike other traditional optical imaging techniques (e.g., confocal microscopy and optical coherence tomography)[8-15]. Given its lower optical scattering and absorption in tissues, near-infrared (NIR) light (650–950 nm) can penetrate biological tissues deeper than visible light[16]. However, a PA signal is proportional to optical absorption. Therefore, strong optical absorbers in NIR region are highly desired for PAT in deep tissue imaging. Various exogenous optical contrasts with high NIR absorption have been extensively explored to increase sensitivity and specificity, thereby expanding the applications of PAT[17-22].

NIR dyes are widely used as biomarkers for *in vivo* imaging because of the strong absorption in the spectral region from approximately 600 nm to 1000 nm. Most biomolecules do not absorb and fluorescence does not occur in this region. Thus, NIR dyes are relatively free from intrinsic background interference coming from the body, thereby significantly enhancing their selectivity. NIR-absorbing indocyanine green (ICG) has been approved by the U.S. Food and Drug Administration (FDA) for clinical applications in human medical imaging and diagnosis[23,24]. ICG is widely employed in clinical applications, such as cardiac output monitoring[25], hepatic function study[26], angiography in ophthalmology[27], and tumor detection[28]. However, the poor stability of ICG in solution limits its clinical applications. In addition, the elimination half-life of ICG after intravenous (i.v.) injection is only 2-4 min because of the natural elimination mechanisms in the human body. Therefore, a delivery system that can provide stability and prolong the life time in

*: These authors contributed equally to this work.
Correspondence to: Zhi-Fei Dai and Chang-Hui Li
E-mail: zhifei.dai@pku.edu.cn and Chli@pku.edu.cn
Received June 6, 2016; accepted July 11, 2016.
Available at www.cancerbiomed.org

physiological solution is of therapeutic interest[29]. Developments in nanotechnology allow the incorporation of ICG into nanoparticle (NP) delivery systems, thereby improving the *in vivo* applications of ICG molecules. Numerous polymeric NPs[30,31] and inorganic NPs[32,33] are recently introduced to address the intrinsic issues of ICG degradation, rapid blood clearance, and *in vivo* imaging.

Degradable superparamagnetic iron oxide (SPIO) NPs are promising candidates for various *in vivo* biomedical applications because of their good biocompatibility. Dextran-coated SPIO NPs have been clinically tested and approved by FDA[34]. Highly monodispersed SPIO NPs can be produced in large quantities by thermal decomposition[35], and the particle surface is most commonly coated with a layer of oleic acid or oleic amine. Film hydration method is usually used to coat magnetic nanocrystals containing small amphiphilic molecules, such as poloxamine and phospholipid-PEG, to improve blood circulation of SPIO NPs[36].

In this study, we used ICG molecules encapsulated in SPIO NPs coated with a lipid layer of 1, 2-distearoyl-sn-glycero-3-phosphoethanolamine-*N*-[methoxy(polyethylene glycol)-2000] (DSPE-PEG2000) as contrast agent to enhance PA imaging and address the rapid clearance and non-specific tissue binding of ICG. Unlike the material without ICG, SPIO@DSPE-PEG/ICG NPs could significantly prolong circulation time *in vivo* and passively accumulated in tumor[37]. PA imaging contrast behaviors *in vitro* (phantom) and *in vivo* (brain vascular and tumor) were also evaluated.

Materials and methods

Materials

ICG, iron(III) acetylacetonate, oleic acid, and oleylamine were purchased from Sigma-Aldrich. Hexane and toluene were obtained from Tianjin Fengchuan Chemical Reagent Science and Technology Co., Ltd. DSPE-PEG2000 was purchased from Avanti Polar Lipids. De-ionized (DI) water (18.2 MU cm) prepared using Milli-Q Gradient System was used in all preparations. All chemicals were of analytical grade and used directly without further purification. MDA-MB-231 cell line was cultured in standard cell media recommended by American Type Culture Collection.

Preparation and characterization of SPIO@DSPE-PEG/ICG NPs

Synthesis of SPIO

NPs were synthesized from the mixture of iron tri (acetylacetonate), oleic acid, and oleylamine according to the previous procedure[38]. In this study, iron tri (acetylacetonate) (0.76 g), oleylamine (1.60 g), oleic acid (1.69 g), and 1, 2-hexadecanediol (2.58 g) were mixed with benzyl ether (20 mL) in a 250-mL three-neck flask. The temperature was increased to 120 °C for 2 h under vacuum. The temperature was subsequently increased to 200 °C within 30 min and kept for another 30 min. The temperature was again increased to 300 °C within 1 h and kept for 30 min. The mixture was subsequently cooled to room temperature and washed three times with ethanol (30 mL) and hexane (15 mL). The deposit was finally dissolved in toluene and stored at room temperature.

Synthesis of SPIO@DSPE-PEG2000

The hydrophobic SPIO NP cores were coated with DSPE-PEG 2000 following the dual solvent exchange method[39]. Briefly, SPIO and DSPE-PEG2000 were dissolved in chloroform at 1:2 weight ratio followed by gradual addition of four volumes of DMSO into the mixture. After complete vaporization of chloroform under vacuum, four volumes of water were added into the mixture. The DMSO was then substituted by water using an ultrafiltration centrifugal device with polyethersulfone membrane (100 kDa cutoff size). Empty micelles were subsequently removed by ultracentrifugation at 100,000×g. The deposit was finally dissolved in water and stored at 4 °C. Iron concentration in toluene and DI water was measured by an inductive coupled plasma emission spectrometer.

Synthesis of SPIO@DSPE-PEG2000/ICG

ICG and SPIO@DSPE-PEG NPs were mixed in water solution at a 1:5 weight ratio. The mixture was stirred overnight at 25 °C, followed by the removal of unloaded ICG molecules by ultracentrifugation at 100,000×g for three times according to literature[40]. The SPIO@DSPE-PEG/ICG deposit was dissolved in ddH_2O and stored at 4 °C.

Encapsulation efficiency and loading capacity of ICG

ICG water solution (1, 10, 20, and 50 μL) at 1 mg/mL concentration was mixed with 100 μg (iron content) SPIO NPs coated with DSPE-PEG 2000. The mixture was placed on a shaker and incubated overnight at room temperature. The unloaded ICG molecules were removed by ultracentrifugation at 100 000×g. ICG encapsulation efficiency (EE) and loading capacity (LC) of SPIO@DSPE-PEG NPs were calculated according to the following equations:

EE=(Mass of encapsulated ICG/Total mass of added

ICG)×100%

LC=(Mass of encapsulated ICG/Mass of iron)×100%

Characterization of SPIO@DSPE-PEG/ICG NPs

The obtained NPs were observed with Hitachi 3600 transmission electron microscope (TEM) connected to a CCD camera. The UV-visible-NIR absorption spectra of SPIO@DSPE-PEG/ICG NPs and that without ICG were analyzed by a UV-visible-NIR spectrophotometer (Varian40 Cary 4000) with a quartz cuvette of 1 cm optical path length.

PAT imaging setup

Three PAT systems were used in this study. A homemade PA computed tomography (PACT) system was used for phantom and brain imaging, a homemade PA microscopy (PAM) was used to compare the circulation time in nude mice, and a real-time multispectral optoacoustic tomographic (MSOT) imaging system (inVision 128, iThera Medical GmbH, Neuherberg, Germany) was used for tumor imaging. In PACT and PAM, a pumped tunable Ti: sapphire laser (LT-2211A, LOTIS TII, Minsk, Belarus) at 808 nm and 10 Hz repetition rate was used to excite PA signals.

In PACT, a laser beam passed through a ground glass and then vertically illuminated the samples. The incident energy density of the laser beam on the surface of test samples was controlled to be less than 10 mJ/cm^2. An unfocused ultrasonic transducer with 2.25 MHz central frequency was used to detect ultrasound signals generated from the samples. The samples and the transducer were immersed in water. The transducer was driven by a step motor to scan horizontally and continuously along a circular path with 12 cm diameter around the sample for 6 min. The PA signals detected by the transducer were amplified and then recorded by an oscilloscope at a sampling rate of 10 MHz. Details of the setup were previously described[17,41]. Two-dimension PA images were reconstructed using a temporal back-projection algorithm, and the contrast-to-noise ratio (CNR), the signal-to-noise tatio (SNR), and noise-equivalent sensitivity were determined following the previous method[42].

In PAM, laser light was delivered through a multi-mode fiber and passed through a dark-field alignment to illuminate the surface of the object. A focused transducer with central frequency of 20 MHz was used to detect ultrasonic signals from the samples. The signals were subsequently amplified and acquired by a data acquisition card at a sampling rate of 200 MHz. The transducer scanned in x-y plane direction above the skin. More details of the setup were previously reported [43].

Imaging gel embedded in chicken breast tissues

Five agar gel cylinders containing SPIO@DSPE-PEG/ICG NPs were embedded in agar gel with a diameter of 2.5 cm and placed under pieces of chicken breast to determine the maximum imaging depth. The concentrations of SPIO@DSPE-PEG/ICG NPs in the five agar gel cylinders were 10, 20, 50, 100, and 200 μg/mL, which were sequentially embedded counterclockwise starting at 12 o'clock direction. Moreover, two carbon rods were placed in the same horizontal plane as the agar objects at the center and 11 o'clock direction as references. The setup and procedure for this experiment are shown in the previous section. Two-dimension imaging of the phantom containing the embedded objects was reconstructed, and blocks of chicken breast were sequentially stacked on the phantom to set the embedded objects at desired depths.

In vivo imaging of mouse brain vasculature

All animals were purchased from Beijing Vital River Laboratories, and all experiments involving animals were performed in accordance with the guidelines of the Institutional Animal Care and Use Committee of Peking University. Kunming mice (~20 g, male) were used for *in vivo* PA imaging of mouse brain. The mice used for imaging were anesthetized, and the fur on their heads was removed before imaging. A thin layer of ultrasonic coupling gel was applied on the surface of the head, and then the mouse was set on an animal bed. Anesthesia was maintained throughout the experiment by an isoflurane machine (0.8%-1.0% vaporized isoflurane with an airflow rate of 1 L/min). The head of the mouse was placed into a water tank through a hole at the bottom. The hole was sealed with a piece of transparent polyethylene film, and the mouse head with gel was in direct contact with the film. Exciting laser pulses were shone vertically onto the mouse head. Control scanning was performed before injecting the contrast agent. Afterward, SPIO@DSPE-PEG/ICG NPs (150 μL with 0.2 mg/mL of ICG) were injected into the mouse tail vein and PAT scanning was performed at a predetermined time.

Comparison of circulation time in nude mice

Monitoring using PAM confirms that the circulation time of SPIO@DSPE-PEG/ICG NPs *in vivo* was longer than that of

ICG. The animal models used were 20 g Balb/c nude mice. Ultrasonic gel was applied on the outer side of a mouse leg, and then similar concentration of ICG and SPIO@DSPE-PEG/ICG NPs (150 μL with 0.2 mg/mL of ICG) were separately injected into two mice through their tail veins. In the PAM experiment, 10 B-scans at the same position for each time point were performed with 5-min interval. The 10 B-scans for each time point and the amplitudes of three selected vessels in all mean B-scans were averaged.

Tumor MSOT imaging *in vivo*

Xenograft mice (Balb/c, ~20 g, female) models were established by subcutaneously injecting (5–6)×10^6 MDA-MB-231 cells into the right flank of the mice. Subcutaneous *in vivo* tumor imaging was performed using an MSOT imaging system. Prior to imaging, temperature-controlled water was placed between the mouse and ultrasonic array for ultrasonic coupling. An animal holder with a thin polyethylene membrane was used to prevent direct contact between the mouse and the water, and ultrasonic coupling agent was applied on the mouse skin to eliminate bubbles. Two groups of MDA-MB-231 tumor-bearing mice were i.v. injected separately with SPIO@DSPE-PEG/ICG NPs (150 μL with 0.2 mg/mL of ICG) and that without ICG (150 μL). A volume region of interest (ROI) consisting of transverse slices with a step size of 0.3 mm spanning the tumor region was selected by manual inspection of live MSOT images. Multispectral imaging was performed before injection and 0.5, 1, 3, 6, 24, and 48 h after injection. Images were reconstructed using an offline model-based approach[44].

In vivo monitoring of probe biodistribution

SPIO@DSPE-PEG/ICG NPs (150 μL with 0.2 mg/mL of ICG) was i.v. injected into tumor-bearing mice anaesthetized under isoflurane, and probe biodistribution was monitored over time in different organs using PA imaging. Before image acquisition, a volume ROI consisting of transverse slices with a step size of 0.3 mm spanning from the liver to the lower abdomen was selected by manual inspection of live MSOT images. Furthermore, five excitation wavelengths (680, 700, 750, 833, and 900 nm) were selected for correspondence with the major turning points in the absorption spectra of SPIO@DSPE-PEG/ICG and oxy- and deoxy-hemoglobin. Multispectral imaging was subsequently performed with 10 signal averages per wavelength per transverse slice, before injection, during injection, and 0.5, 1, 3, 6, 24, and 48 h after injection. Images were reconstructed using a model-based approach[44].

Results

Preparation and characterization of ICG-loaded SPIO NPs

Biocompatible and biodegradable SPIO@ SPIO@DSPE-PEG/ICG NPs were constructed using the procedure shown in **Figure 1A**. Hydrophobic SPIO NPs stabilized with oleylamine and oleic acid were coated with DSPE-PEG2000 using the solvent exchange method[38,39]. By mixing 0.2 mg ICG with 1 mg SPIO NPs (mass ratio-1:5), we easily loaded ICG molecules into DSPE-PEG-coated SPIO NPs given the amphiphilic nature of their structure. EE and LC of ICG were as high as 76.5% and 15.3%, respectively. A TEM image reveals that SPIO@DSPE-PEG/ICG NPs exhibited a uniform diameter of ~28 nm (**Figure 1B**), consistent with DLS measurement (**Figure 1D**). SPIO@DSPE-PEG/ICG NPs and that without ICG showed a strong NIR absorption in the NIR region between 750 and 850 nm with a peak at approximately 833 and 780 nm (**Figure 1C**). The high absorption coefficient in the NIR wavelength region guaranteed the potential of SPIO@DSPE-PEG/ICG NPs as an excellent PAT contrast agent. As shown in **Figure 1D**, SPIO@DSPE-PEG/ICG NPs generated a strong PA signal when illuminated by NIR laser pulses at 795 nm. The signal intensities increased linearly with the concentrations of SPIO@DSPE-PEG/ICG and without ICG aqueous solution (**Figure 1E**). Thus, the highly absorbent SPIO@DSPE-PEG/ICG NPs can dominate the relatively weak background solvent spectrum in the NIR region.

In vivo toxicity studies

For further biological applications, the PAT contrast agent must demonstrate high biocompatibility. This property has been proven in previous cell experiment[40]. The potential *in vivo* toxicity of SPIO@DSPE-PEG/ICG NPs in mice was evaluated further based on body weight loss and pathologic changes in representative organs. The analysis was conducted by injecting a single imaging dose of SPIO@DSPE-PEG/ICG NPs (150 μL with 0.2 mg/mL of ICG) through the tail vein. Compared with the untreated group, neither death nor significant body weight drop was observed in any of the experimental animal groups during the study period. This finding indicates that no significant systemic toxicity occurred in SPIO@DSPE-PEG/ICG NP-treated mice. In addition, H&E staining of vital organs (heart, liver, spleen,

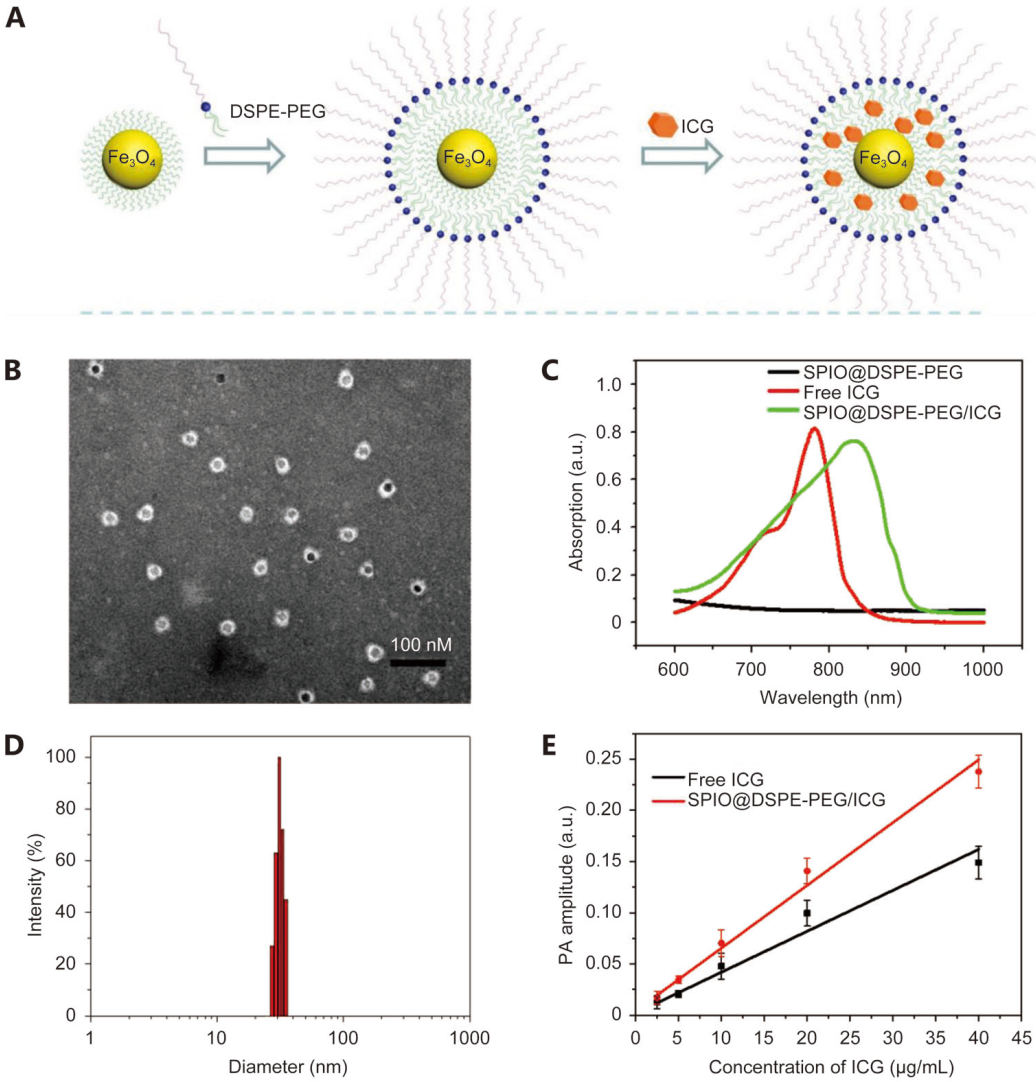

Figure 1 (A) A schematic illustration for SPIO@DSPE-PEG/ICG NPs preparation. (B) The SPIO@DSPE-PEG/ICG NPs had a uniform diameter of average size of 28 nm based on the TEM image. (C) UV-Vis-NIR extinction spectrum of SPIO@DSPE-PEG/ICG NPs free ICG and SPIO@DSPE-PEG NPs in water. (D) The diameter distribution of SPIO@DSPE-PEG/ICG NPs by DLS measurements. (E) Plot of the photoacoustic amplitude as a function of SPIO@DSPE-PEG/ICG NPs solution concentration and free ICG solution.

lungs, and kidneys) did not show any apparent damage in cellular structures 20 days after SPIO@DSPE-PEG/ICG NP injection (**Figure 2**). Thus, SPIO@DSPE-PEG/ICG NPs demonstrate good biocompatibility, which is an attractive feature for *in vivo* applications of PAT.

PAT phantom study

We aimed to verify the feasibility of SPIO@DSPE-PEG/ICG NPs as PAT contrast agent and to determine their effective imaging depth at 808 nm wavelength. Thus, we used a 2.25-MHz ultrasonic transducer to obtain PA tomographic images *in vitro* of a tissue-mimicking phantom, which was made of agar gel embedding SPIO@DSPE-PEG/ICG NPs and placed under ~1.0 cm-thick chicken breast (**Figure 3A**). **Figure 3B-F** show the PAT images of the phantom under pieces of chicken breast at depths of 0, 0.8, 2.1, 2.9 and 3.9 cm. All the agar gel cylinders were clearly visualized at 0.8 cm depth, indicating that SPIO@DSPE-PEG/ICG NPs demonstrated an excellent PAT imaging capability. The PA intensities of 200 μg/mL SPIO@DSPE-PEG/ICG NP-containing gels derived from the reconstructed images at different depths were subsequently calibrated according to the signal amplifications employed in the experiment. The NIR light weakened as the

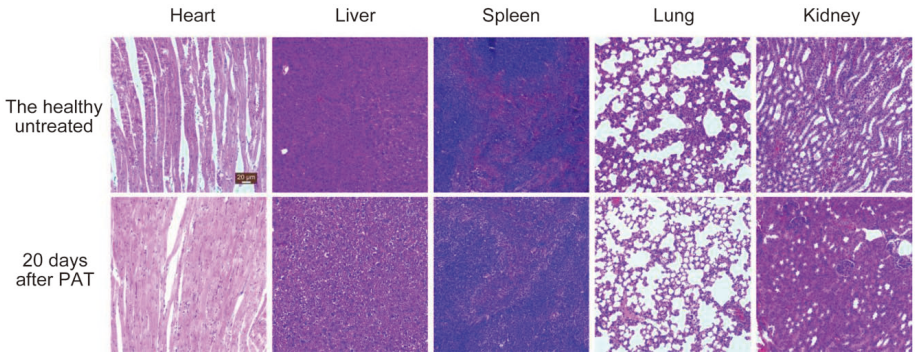

Figure 2 Micrographs of H&E stained organ slices from the healthy untreated and SPIO@DSPE-PEG/ICG treated group at 20 days after treatment (H&E staining, 40×).

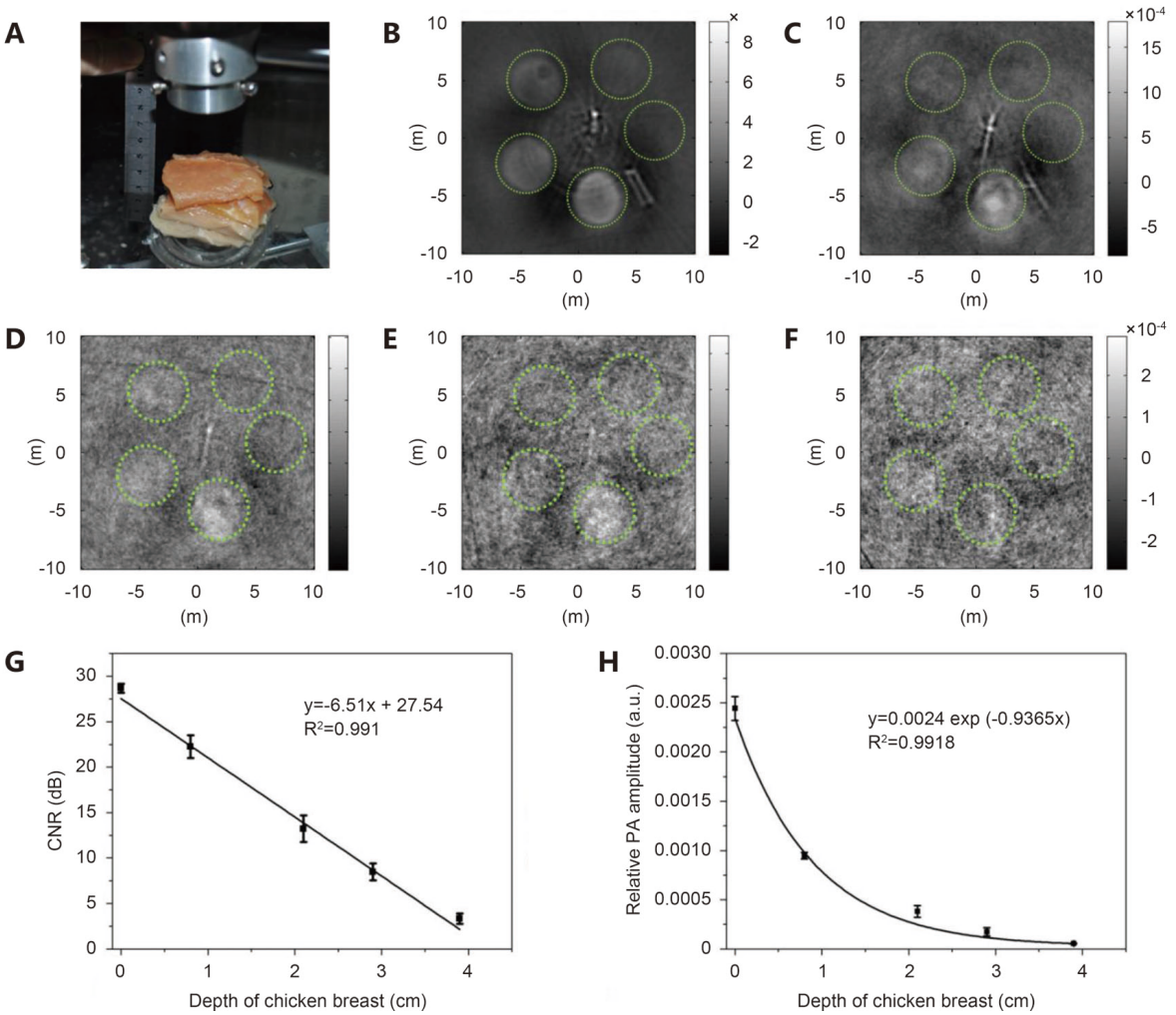

Figure 3 Agar gels containing SPIO@DSPE-PEG/ICG NPs were embedded in an agar phantom, which was then placed under varying numbers of pieces of chicken breast. (A) Photoacoustic imaging device. A two-dimensional photoacoustic image at a depth of 0 cm (B), 0.8 cm (C), 2.1 cm (D), 2.9 cm (E) and 3.9 cm (F), respectively. (G) 100 μg/mL SPIO@DSPE-PEG/ICG NPs plot of CNR in decibels as a function of depth of chicken breast. (H) Experimental photoacoustic signal intensity of 100 μg/mL SPIO@DSPE-PEG/ICG NPs contained in agar gel embedded in chicken breast measured at a wavelength of 808 nm as a function of depth from the laser-illuminated surface.

depth of the chicken breast increased because of light scattering and the adsorption by chicken breast; consequently, the CNR in decibels of the reconstructed image decreased linearly with increasing depth (**Figure 3G**). The measured penetration depth for 1/e decay in chicken breast tissue was approximately 1.07 cm at 808 nm wavelength (**Figure 3H**). At the maximum imaging depth of 2.9 cm achieved in our experiment, the 200 μg/mL SPIO@DSPE-PEG/ICG NP-containing gels (Fe content is 200 μg/mL) still showed excellent CNR. All these results demonstrate that SPIO@DSPE-PEG/ICG NPs are promising agents that can enhance PA contrast and can be applied in non-invasive *in vivo* tumor imaging.

Comparison of circulation time in nude mice

To confirm that the circulation time of SPIO@DSPE-PEG/ICG NPs was longer than that of the material without ICG, we studied the time-dependent variation attributable to contrast agents in optical absorption in mouse leg vessels *in vivo* (**Figure 4**). The results show that the clearance of the material without ICG from the circulatory system lasted for approximately 30 min, whereas SPIO@DSPE-PEG/ICG NPs did not show an obvious clearance from the circulatory system within 90 min.

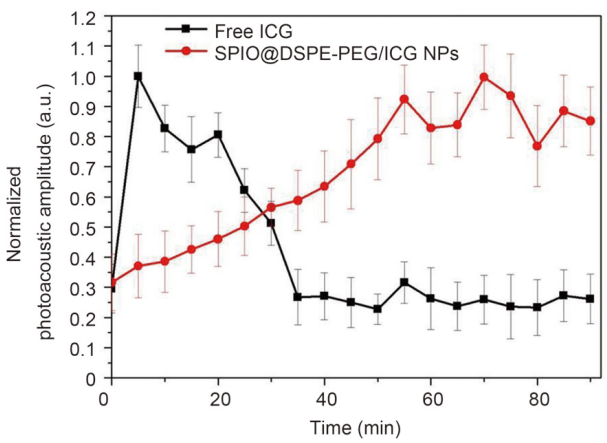

Figure 4 Intensity of the photoacoustic signals from leg vessels of the mouse as a function of time after the intravascular injection of SPIO@DSPE-PEG/ICG NPs (red) or free ICG (black), which are normalized to the maximum intensity of the photoacoustic signals after the injection.

In vivo PAT imaging of cerebral cortex vessels of Kunming mouse

The cerebral cortex of a mouse was imaged before and after a single injection of SPIO@DSPE-PEG/ICG NPs (150 μL with 0.2 mg/mL of ICG) using PAT at 808 nm (**Figure 5**). Compared with the brain image based on intrinsic optical contrast (**Figure 5A**), the image obtained 15 min after administration of SPIO@DSPE-PEG/ICG NPs shows clearer brain vasculature (**Figure 5B**). The circulating SPIO@DSPE-PEG/ICG NPs in blood enhanced the PA signals of the blood vessels, demonstrating a good contrast performance of SPIO@DSPE-PEG/ICG NPs. This result is better appreciated in a differential image (**Figure 5D**) obtained by subtracting the pre-injection image (**Figure 5A**) from the post-injection image (**Figure 5B**) by pixels. At 1 h after the injection, the PA signal remained essentially intensive, indicating a sufficient amount of SPIO@DSPE-PEG/ICG NPs circulating in the blood (**Figures 5C** and **E**). Therefore, our results prove that distribution of long-circulating SPIO@DSPE-PEG/ICG NPs in the vasculature can conduct and enhance PA imaging of brain vessels in live mice with intact skin and skull.

In vivo PAT imaging of tumor

MSOT tumor imaging was used to explore the tumor targeting capability of SPIO@DSPE-PEG/ICG NPs in nude mice. PA images were collected before and after a single intravenous injection of SPIO@DSPE-PEG/ICG NPs. As shown in **Figure 6**, prior to intravenous injection of SPIO@DSPE-PEG/ICG NPs (150 μL with 0.2 mg/mL of ICG), the background PA intensity (gray) of tumor was relatively high because of the absence of oxy- and deoxy-hemoglobin. **Figure 6A** shows that the SPIO@DSPE-PEG/ICG NP signal (green) was rather weak. An inhomogeneous distribution of the contrast agent within the tumor was observed 1, 6, and 24 h after injection. The overall PA signal in the tumor region nearly peaked within 6 h, suggesting that large amounts of SPIO@DSPE-PEG/ICG NPs circulated in the blood and then accumulated at the tumor site. **Figure 6B** shows that the tumor-to-muscle ratio of the MSOT signal peaked at the 6-h time point, demonstrating the accumulation of SPIO@DSPE-PEG/ICG NP at the tumor site.

In vivo monitoring of probe biodistribution

In vivo biodistribution of SPIO@DSPE-PEG/ICG NPs was investigated using MSOT imaging. **Figure 7** shows that, in the first 1 h, the SPIO@DSPE-PEG/ICG NPs were highly distributed in the spleen, liver, and kidney. However, in the subsequent time points, the SPIO@DSPE-PEG/ICG NPs in the spleen, liver, and kidney were quickly cleared and mainly accumulated in the tumor site, and then peaked at 6 h. This finding is consistent with the result of MSOT tumor imaging.

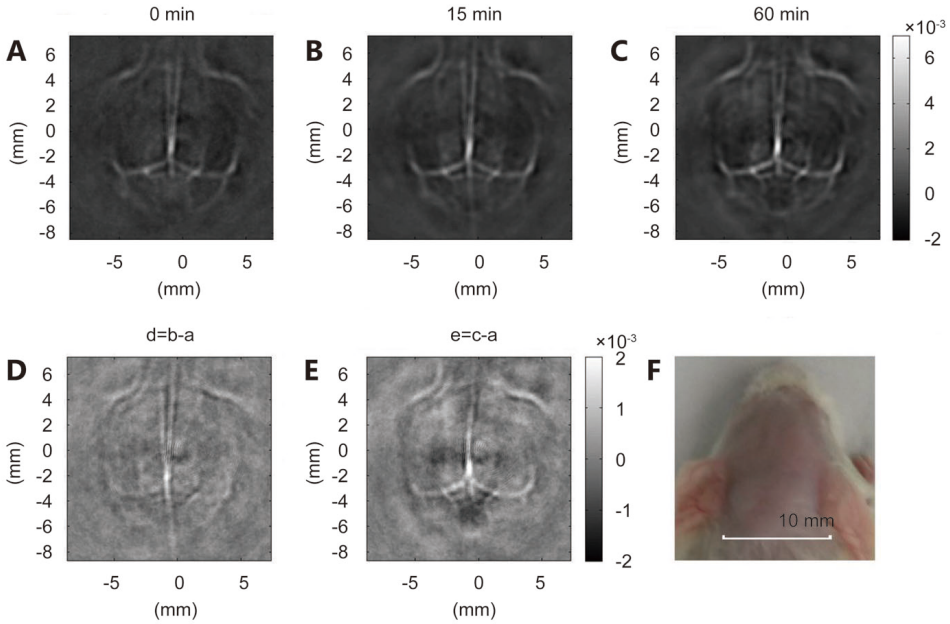

Figure 5 Non-invasive PAT imaging of a mouse brain *in vivo* employing SPIO@DSPE-PEG/ICG NPs and NIR light at a wavelength of 808 nm. Photoacoustic image acquired before (A), at 15 min (B), and 60 min (C) after the intravenous injection of SPIO@DSPE-PEG/ICG NPs. (D and E) Differential images that were obtained by subtracting the pre-injection image from the post-injection images (image D-image B-image A; image E-image C-image A). (F) Photograph of the mouse brain obtained before the data acquisition for PAT.

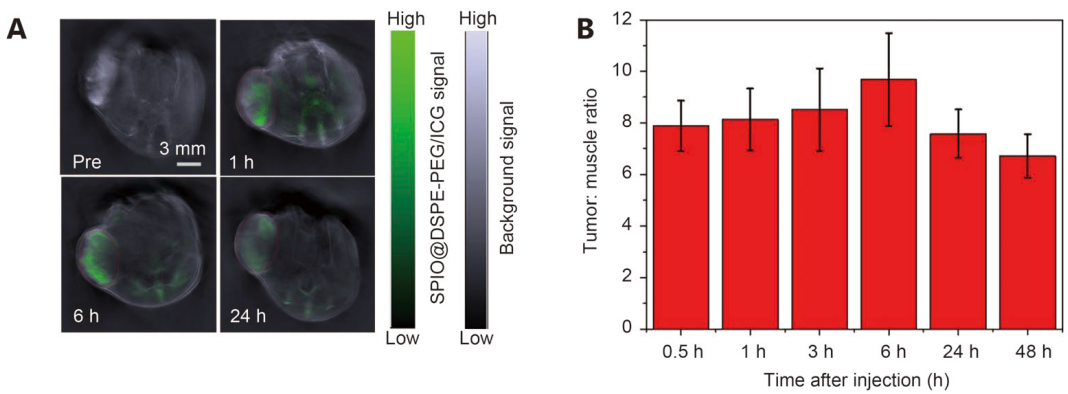

Figure 6 (A) PA images collected by MOST imaging system before (pre) and at different time points (1 h, 6 h, 24 h) after the intravenous injection of SPIO@DSPE-PEG/ICG NPs. (B) Tumor-to-muscle ratios of MSOT signal at multiple time points (n=3).

Discussion

PAT has attracted extensive interest owing to its high optical absorption contrast with superior ultrasonic resolution. Various NIR NPs, such as gold nanostructures, copper sulfide NPs, and carbon nanotubes, have been evaluated as potential contrast agents for PAT imaging. However, none of them can fully satisfy the requirements for PAT imaging. These NIR NPs are disadvantageous in that they are non-biodegradable and are retained over time in different organs, thereby raising the potential risk of toxicity. Such NPs cannot be used for clinical diagnosis in the near future.

In the present study, we confirmed that SPIO@DSPE-PEG/ICG NPs are promising contrast agents for PAT in clinical applications in humans. Considering that ICG and SPIO NPs are FDA-approved drugs, we designed SPIO@DSPE-PEG/ICG NPs and used them as biodegradable and biocompatible contrast agents for PAT. The obtained

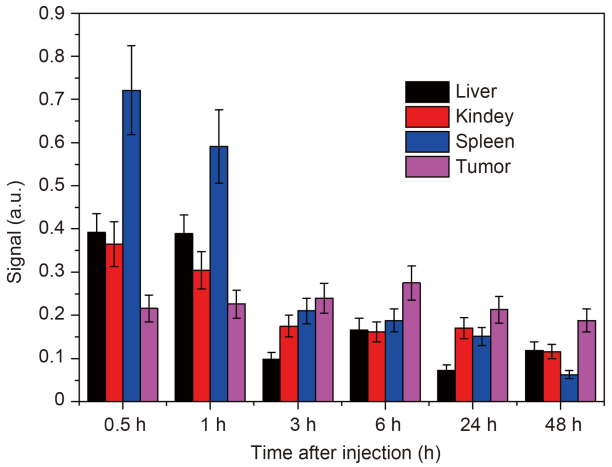

Figure 7 Biodistribution of SPIO@DSPE-PEG/ICG at different organs and tumor at different time points.

SPIO@DSPE-PEG/ICG NPs can offer long-term blood circulation. Polyethylene glycol coating on the surface SPIO NPs can effectively reduce protein adsorption *in vivo*, thereby avoiding macrophage recognition by reticuloendothelial system (RES). Thus, encapsulation of ICG molecules by a lipid layer can protect them from rapid degradation. The ideal diameter of NP for i.v. administration to increase circulation time in blood stream is 10–50 nm[45,46] given that larger or smaller NPs tend to be removed by RES or by the renal system, respectively[47,48]. Therefore, a diameter of 28 nm (**Figure 1B**) is appropriate to ensure the potential *in vivo* applications of SPIO@DSPE-PEG/ICG NPs. The *in vivo* experiments show that SPIO@DSPE-PEG/ICG NPs demonstrated a considerably longer blood circulation time than that without ICG (**Figure 4**). The designed NPs also displayed strong tumor targeting capability without being retained in major organs, such as spleen, liver, and kidney (**Figure 7**). At the time points after 1 h after the injection, the tumor showed a high tumor/muscle ratio (**Figure 6B**) and displayed the maximum MSOT signal among the organs (**Figure 7**). Therefore, SPIO@DSPE-PEG/ICG NPs can be applied in tumor diagnosis.

Similar to that without ICG (**Figure 1C**), the same concentration of SPIO@DSPE-PEG/ICG NPs showed a maximum absorption and red spectral shift of 53 nm (from 780 nm to 833 nm) in aqueous solution. This result is attributed to the hydrophobic characteristic of the environment where the ICG molecules reside and the relatively high local concentration. In the case of fluorescent dyes, a low quantum yield results in an efficient PA signal generation because a great amount of the absorbed energy is converted into PA signal instead of being emitted. A high local ICG concentration of SPIO@DSPE-PEG/ICG NPs resulted in a low quantum yield because of fluorescence quenching, demonstrating a strong PA transfer capability of SPIO@DSPE-PEG/ICG NPs (**Figure 1E**). The *in vivo* experiments also show that the use of NIR light at 833 nm wavelength is more suitable for PA tissue imaging owing to its strong capability for tissue penetration than that at 780 nm.

Although ICG can be easily loaded into a lipid core by simply mixing ICG and SPIO@DSPE-PEG2000 in a water solution given the amphiphilic nature of the latter, quick release of ICG from the SPIO@DSPE-PEG2000 after injection into the body is possible. However, SPIO@DSPE-PEG/ICG showed a considerably longer blood circulation time than that without ICG did (**Figure 4**), successful accumulation in tumor, and could be retained for at least 24 h (**Figure 6** and **7**). By contrast, after injection of that without ICG, PA signal enhancement was observed in the liver only in the first hour, and no PA signal enhancement occurred in the tumor. These experimental results demonstrate that the loaded ICG were retained in the hydrophobic region instead of being released into the surrounding hydrophilic environment. The reason is that ICG molecules were cleared immediately as soon as they were released into the surrounding hydrophilic environment. Thus, ICG can stably stay in the hydrophobic region possibly because the ICG structure is hydrophobic and ICG tends to be distributed in the hydrophobic region. This phenomenon may also explain its relatively high LC and EE.

In summary, we demonstrated that SPIO@DSPE-PEG/ICG NPs can be an excellent contrast agent to enhance PA imaging *in vitro* and *in vivo* resulting from strong absorption of NIR light, which allows deeper penetration of laser light and lowers the intrinsic background from hemoglobin. The *in vivo* PAT imaging shows the long circulation time and the high tumor targeting efficiency of SPIO@DSPE-PEG/ICG NPs. In addition to the reported capabilities of enhancing magnetic imaging and fluorescence imaging *in vivo*[40], the multimodal SPIO@DSPE-PEG/ICG NPs may offer a new approach to accurately interpret obtained images and identify the size and location of tumors. Such features are useful in determining tumor margins. Moreover, the combination of two clinically approved components to form this novel agent can offer large potential in clinical applications.

Acknowledgments

This work was supported by National Key Research and Development Program of China (Grant No. 2016YFA0201400), State Key Program of National Natural Science of China (Grant No. 81230036), National Natural Science Foundation for Distinguished Young Scholars (Grant No. 81225011), National Natural Science Foundation of China (Grant No. 21273014) and the Foundation for Innovative Research Groups of the National Natural Science Foundation of China (Grant No. 81421004).

Conflict of interest statement

No potential conflicts of interest are disclosed.

References

1. Wang LHV, Hu S. Photoacoustic tomography: In vivo imaging from organelles to organs. Science. 2012; 335: 1458-62.
2. Li CH, Wang LHV. Photoacoustic tomography and sensing in biomedicine. Phys Med Biol. 2009; 54: R59-97.
3. Yang S, Xing D, Zhou Q, Xiang L, Lao Y. Functional imaging of cerebrovascular activities in small animals using high-resolution photoacoustic tomography. Med Phys. 2007; 34: 3294-301.
4. Chen ZJ, Yang SH, Xing D. In vivo detection of hemoglobin oxygen saturation and carboxyhemoglobin saturation with multiwavelength photoacoustic microscopy. Opt Lett. 2012; 37: 3414-16.
5. Song KH, Kim CH, Cobley CM, Xia YN, Wang LV. Near-infrared gold nanocages as a new class of tracers for photoacoustic sentinel lymph node mapping on a rat model. Nano Lett. 2009; 9: 183-8.
6. Kim JW, Galanzha EI, Shashkov EV, Moon HM, Zharov VP. Golden carbon nanotubes as multimodal photoacoustic and photothermal high-contrast molecular agents. Nat Nanotechnol. 2009; 4: 688-94.
7. Lao YQ, Xing D, Yang SH, Xiang LZ. Noninvasive photoacoustic imaging of the developing vasculature during early tumor growth. Phys Med Biol. 2008; 53: 4203-12.
8. Xu MH, Wang LHV. Photoacoustic imaging in biomedicine. Rev Sci Instrum. 2006; 77: 041101
9. Oh JT, Li ML, Zhang HF, Maslov K, Stoica G, Wang LHV. Three-dimensional imaging of skin melanoma in vivo by dual-wavelength photoacoustic microscopy. J Biomed Opt. 2006; 11: 034032
10. Zhang HF, Maslov K, Stoica G, Wang LHV. Imaging acute thermal burns by photoacoustic microscopy. J Biomed Opt. 2006; 11: 054033-054033
11. Wang XD, Xie XY, Ku GN, Wang LHV. Noninvasive imaging of hemoglobin concentration and oxygenation in the rat brain using high-resolution photoacoustic tomography. J Biomed Opt. 2006; 11: 024015-024015
12. Zhang HF, Maslov K, Stoica G, Wang LHV. Functional photoacoustic microscopy for high-resolution and noninvasive in vivo imaging. Nat Biotechnol. 2006; 24: 848-51.
13. Manohar S, Vaartjes SE, van Hespen JCG, Klaase JM, van den Engh FM, Steenbergen W, et al. Initial results of in vivo non-invasive cancer imaging in the human breast using near-infrared photoacoustics. Opt Express. 2007; 15: 12277-85.
14. Ermilov S, Stein A, Conjusteau A, Gharieb R, Lacewell R, Miller T, et al. Detection and noninvasive diagnostics of breast cancer with two-color laser optoacoustic imaging system. Proc Spie. 2007; 6437: 643703
15. Ku G, Wang LHV. Deeply penetrating photoacoustic tomography in biological tissues enhanced with an optical contrast agent. Opt Lett. 2005; 30: 507-9.
16. Smith AM, Mancini MC, Nie SM. Bioimaging second window for in vivo imaging. Nat Nanotechnol. 2009; 4: 710-1.
17. Wang YW, Xie XY, Wang XD, Ku G, Gill KL, O'Neal DP, et al. Photoacoustic tomography of a nanoshell contrast agent in the in vivo rat brain. Nano Lett. 2004; 4: 1689-92.
18. Qin H, Zhou T, Yang SH, Xing D. Fluorescence quenching nanoprobes dedicated to in vivo photoacoustic imaging and high-efficient tumor therapy in deep-seated tissue. Small. 2015; 11: 2675-86.
19. Qin H, Zhou T, Yang SH, Chen Q, Xing D. Gadolinium(iii)-gold nanorods for mri and photoacoustic imaging dual-modality detection of macrophages in atherosclerotic inflammation. Nanomedicine-Uk. 2013; 8: 1611-24.
20. Chen YS, Frey W, Kim S, Kruizinga P, Homan K, Emelianov S. Silica-coated gold nanorods as photoacoustic signal nanoamplifiers. Nano Lett. 2011; 11: 348-54.
21. Kim C, Cho EC, Chen JY, Song KH, Au L, Favazza C, et al. In vivo molecular photoacoustic tomography of melanomas targeted by bioconjugated gold nanocages. Acs Nano. 2010; 4: 4559-64.
22. De La Zerda A, Zavaleta C, Keren S, Vaithilingam S, Bodapati S, Liu Z, et al. Carbon nanotubes as photoacoustic molecular imaging agents in living mice. Nat Nanotechnol. 2008; 3: 557-62.
23. Desmettre T, Devoisselle JM, Mordon S. Fluorescence properties and metabolic features of indocyanine green (icg) as related to angiography. Surv Ophthalmol. 2000; 45: 15-27.
24. Yu J, Yaseen MA, Anvari B, Wong MS. Synthesis of near-infrared-absorbing nanoparticle-assembled capsules. Chem Mater. 2007; 19: 1277-84.
25. He YL, Tanigami H, Ueyama H, Mashimo T, Yoshiya I. Measurement of blood volume using indocyanine green measured with pulse-spectrophotometry: Its reproducibility and reliability. Crit Care Med. 1998; 26: 1446-51.
26. Caesar J, Shaldon S, Chiandussi Le, Guevara L, Sherlock S. The use of indocyanine green in the measurement of hepatic blood flow and as a test of hepatic function. Clin Sci. 1961; 21: 43.
27. Hochheimer BF. Angiography of the retina with indocyanine green. Archives of Ophthalmology. 1971; 86: 564-5.
28. Haglund MM, Berger MS, Hochman DW. Enhanced optical imaging of human gliomas and tumor margins. Neurosurgery.

1996; 38: 308-17.

29. Cherrick GR, Stein SW, Leevy CM, Davidson CS. Indocyanine green: Observations on its physical properties, plasma decay, and hepatic extraction. J Clin Invest. 1960; 39: 592.
30. Stover TC, Sharma A, Robertson GP, Kester M. Systemic delivery of liposomal short-chain ceramide limits solid tumor growth in murine models of breast adenocarcinoma. Clin Cancer Res. 2005; 11: 3465-74.
31. Sandanaraj BS, Gremlich HU, Kneuer R, Dawson J, Wacha S. Fluorescent nanoprobes as a biomarker for increased vascular permeability: Implications in diagnosis and treatment of cancer and inflammation. Bioconjugate Chem. 2010; 21: 93-101.
32. Morgan TT, Muddana HS, Altinoglu EI, Rouse SM, Tabakovic A, Tabouillot T, et al. Encapsulation of organic molecules in calcium phosphate nanocomposite particles for intracellular imaging and drug delivery. Nano Lett. 2008; 8: 4108-15.
33. Altinoglu EI, Russin TJ, Kaiser JM, Barth BM, Eklund PC, Kester M, et al. Near-infrared emitting fluorophore-doped calcium phosphate nanoparticles for in vivo imaging of human breast cancer. Acs Nano. 2008; 2: 2075-84.
34. Tassa C, Shaw SY, Weissleder R. Dextran-coated iron oxide nanoparticles: A versatile platform for targeted molecular imaging, molecular diagnostics, and therapy. Accounts Chem Res. 2011; 44: 842-52.
35. Park J, An KJ, Hwang YS, Park JG, Noh HJ, Kim JY, et al. Ultra-large-scale syntheses of monodisperse nanocrystals. Nat Mater. 2004; 3: 891-5.
36. Dubertret B, Skourides P, Norris DJ, Noireaux V, Brivanlou AH, Libchaber A. In vivo imaging of quantum dots encapsulated in phospholipid micelles. Science. 2002; 298: 1759-62.
37. Maeda H, Fang J, Inutsuka T, Kitamoto Y. Vascular permeability enhancement in solid tumor: Various factors, mechanisms involved and its implications. Int Immunopharmacol. 2003; 3: 319-28.
38. Tong S, Hou SJ, Zheng ZL, Zhou J, Bao G. Coating optimization of superparamagnetic iron oxide nanoparticles for high t-2 relaxivity. Nano Lett. 2010; 10: 4607-13.
39. Tong S, Hou SJ, Ren BB, Zheng ZL, Bao G. Self-assembly of phospholipid-peg coating on nanoparticles through dual solvent exchange. Nano Lett. 2011; 11: 3720-26.
40. Ma Y, Tong S, Bao G, Gao C, Dai ZF. Indocyanine green loaded spio nanoparticles with phospholipid-peg coating for dual-modal imaging and photothermal therapy. Biomaterials. 2013; 34: 7706-14.
41. Yang XM, Skrabalak SE, Li ZY, Xia YN, Wang LHV. Photoacoustic tomography of a rat cerebral cortex in vivo with au nanocages as an optical contrast agent. Nano Lett. 2007; 7: 3798-802.
42. Xu MH, Wang LHV. Pulsed-microwave-induced thermoacoustic tomography: Filtered backprojection in a circular measurement configuration. Med Phys. 2002; 29: 1661-9.
43. Ye SQ, Yang JY, Xi JZ, Ren QS, Li CH. Studying murine hindlimb ischemia by photoacoustic microscopy. Chin Opt Lett. 2012; 10: 121701-121701.
44. Rosenthal A, Razansky D, Ntziachristos V. Fast semi-analytical model-based acoustic inversion for quantitative optoacoustic tomography. Ieee T Med Imaging. 2010; 29: 1275-85.
45. Choi HS, Liu W, Misra P, Tanaka E, Zimmer JP, Ipe BI, et al. Renal clearance of quantum dots. Nat Biotechnol. 2007; 25: 1165-70.
46. Jiang W, Kim BYS, Rutka JT, Chan WCW. Nanoparticle-mediated cellular response is size-dependent. Nat Nanotechnol. 2008; 3: 145-50.
47. Osaki F, Kanamori T, Sando S, Sera T, Aoyama Y. A quantum dot conjugated sugar ball and its cellular uptake on the size effects of endocytosis in the subviral region. J Am Chem Soc. 2004; 126: 6520-1.
48. De Jong WH, Hagens WI, Krystek P, Burger MC, Sips AJAM, Geertsma RE. Particle size-dependent organ distribution of gold nanoparticles after intravenous administration. Biomaterials. 2008; 29: 1912-19.

Cite this article as: Gao C, Deng Z, Peng D, Jin Y, Ma Y, Li Y, et al. Near-infrared dye-loaded magnetic nanoparticles as photoacoustic contrast agent for enhanced tumor imaging. Cancer Biol Med. 2016; 13: 349-59. doi: 10.20892/j.issn.2095-3941.2016.0048